

# Chemical Imaging of Mixed Metal Oxide Catalysts for Propylene Oxidation: From Model Binary Systems to Complex Multicomponent Systems

Paul Sprenger,<sup>[a]</sup> Matthias Stehle,<sup>[a]</sup> Abhijeet Gaur,<sup>[a, b]</sup> Jana Weiß,<sup>[c]</sup> Dennis Brueckner,<sup>[d, e, f]</sup> Yi Zhang,<sup>[d]</sup> Jan Garrevoet,<sup>[d]</sup> Jussi-Petteri Suuronen,<sup>[g, h]</sup> Michael Thomann,<sup>[i]</sup> Achim Fischer,<sup>[i]</sup> Jan-Dierk Grunwaldt,<sup>\*[a, b]</sup> and Thomas L. Sheppard<sup>\*[a, b]</sup>

Industrially-applied mixed metal oxide catalysts often possess an ensemble of structural components with complementary functions. Characterisation of these hierarchical systems is challenging, particularly moving from binary to quaternary systems. Here a quaternary Bi–Mo–Co–Fe oxide catalyst showing significantly greater activity than binary Bi–Mo oxides for selective propylene oxidation to acrolein was studied with chemical imaging techniques from the microscale to nanoscale. Conventional techniques like XRD and Raman spectroscopy could only distinguish a small number of components. Spatially-resolved characterisation provided a clearer picture of

metal oxide phase composition, starting from elemental distribution by SEM-EDX and spatially-resolved mapping of metal oxide components by 2D Raman spectroscopy. This was extended to 3D using multiscale hard X-ray tomography with fluorescence, phase, and diffraction contrast. The identification and co-localisation of phases in 2D and 3D can assist in rationalising catalytic performance during propylene oxidation, based on studies of model, binary, or ternary catalyst systems in literature. This approach is generally applicable and attractive for characterisation of complex mixed metal oxide systems.

## Introduction

Mixed metal oxides (MMOs) are involved in many heterogeneous catalytic processes for industrial synthesis of specialty chemicals,<sup>[1]</sup> and are prominently applied in selective oxidation of hydrocarbons.<sup>[2–4]</sup> For example, quaternary Bi–Mo–Co–Fe oxide catalysts are especially relevant for propylene oxidation to acrolein and acrylic acid.<sup>[5]</sup> Acrylic acid alone is a major commodity chemical with global production on the scale of several megatons per year. MMO catalysts often show remarkable enhancements in catalytic performance through cooperation of their different structural components, and can be

visualised as heterogeneous ensembles of crystalline and amorphous oxide phases intermixed on at least the micrometre scale.<sup>[6–7]</sup> Due to this high complexity, simplified particle models and characterisation of model binary systems have historically been used to illustrate and predict the interaction of individual MMO phases.<sup>[8–10]</sup> The present understanding of Bi–Mo–Co–Fe oxide interactions is: 1) bismuth molybdates ( $\alpha$ -Bi<sub>2</sub>Mo<sub>3</sub>O<sub>12</sub>,  $\beta$ -Bi<sub>2</sub>Mo<sub>2</sub>O<sub>9</sub> and  $\gamma$ -Bi<sub>2</sub>MoO<sub>6</sub>) enable selective propylene oxidation, 2) iron molybdates (FeMoO<sub>4</sub>/Fe<sub>2</sub>Mo<sub>3</sub>O<sub>12</sub>) improve the availability of lattice oxygen at the reactive centres, and 3) cobalt molybdates ( $\alpha$ -CoMoO<sub>4</sub> and  $\beta$ -CoMoO<sub>4</sub>) act as a host structure or support phase.<sup>[9,11]</sup> However, the precise composition and

[a] Dr. P. Sprenger, M. Stehle, Dr. A. Gaur, Prof. J.-D. Grunwaldt, Dr. T. L. Sheppard  
Institute for Chemical Technology and Polymer Chemistry  
Karlsruhe Institute of Technology  
Karlsruhe 76131 (Germany)  
E-mail: grunwaldt@kit.edu  
thomas.sheppard@kit.edu

[b] Dr. A. Gaur, Prof. J.-D. Grunwaldt, Dr. T. L. Sheppard  
Institute of Catalysis Research and Technology  
Karlsruhe Institute of Technology  
Eggenstein-Leopoldshafen 76344 (Germany)  
E-mail: grunwaldt@kit.edu  
thomas.sheppard@kit.edu

[c] Dr. J. Weiß  
Leibniz Institute for Catalysis (LIKAT)  
Rostock 18059 (Germany)

[d] D. Brueckner, Dr. Y. Zhang, Dr. J. Garrevoet  
Deutsches Elektronen-Synchrotron DESY  
Hamburg 22607 (Germany)


[e] D. Brueckner  
Faculty of Chemistry and Biochemistry  
Ruhr University Bochum  
Bochum 44801 (Germany)


[f] D. Brueckner  
Department Physik  
Universität Hamburg  
Hamburg 22761 (Germany)

[g] Dr. J.-P. Suuronen  
ESRF - The European Synchrotron  
Grenoble 38000 (France)

[h] Dr. J.-P. Suuronen  
Current Address:  
Xploraytion GmbH  
Berlin 10625 (Germany)

[i] Dr. M. Thomann, Dr. A. Fischer  
Evonik Operations GmbH  
Hanau-Wolfgang 63457 (Germany)

 Supporting information for this article is available on the WWW under <https://doi.org/10.1002/cctc.202100054>

 © 2021 The Authors. ChemCatChem published by Wiley-VCH GmbH. This is an open access article under the terms of the Creative Commons Attribution Non-Commercial NoDerivs License, which permits use and distribution in any medium, provided the original work is properly cited, the use is non-commercial and no modifications or adaptations are made.

function of multicomponent catalysts is naturally more complex than particle models or binary systems may suggest. In particular, the potential interaction or cooperative function of specific phases often cannot be accurately determined based on studies of model or binary systems alone. For example, catalytic performance may be influenced also by pure metal oxide phases (e.g.,  $\text{MoO}_3$  or  $\text{CoO}$ ) as well as mixed or intermediate phases (e.g.,  $\text{Fe}_x\text{Co}_{1-x}\text{MoO}_4$  or  $\text{Bi}_3\text{FeMo}_2\text{O}_{12}$ ) that may act as selective, promotor, inert or unselective phases.<sup>[12–13]</sup> Consequently this complicates the collection of meaningful data describing the presence and interaction of individual phases in industrially-relevant systems, such as quaternary MMOs.

In selective propylene oxidation, four-component Bi–Mo–Co–Fe oxide systems are known to show enhanced catalytic activity compared to pure binary bismuth molybdates.<sup>[9,14–15]</sup> At the same time, for MMO catalysts the choice of synthesis method and pre-treatment can strongly impact catalytic performance.<sup>[16–18]</sup> As catalyst complexity increases together with the number of individual metal oxide components present (e.g., from binary bismuth molybdates to quaternary Bi–Mo–Co–Fe oxide systems), the challenge of monitoring the distribution and interaction of the individual MMO components likewise becomes greater. Characterisation of complex quaternary MMOs is therefore recognised as a significant challenge, but also necessary in order to rationalise the often superior catalytic activity and selectivity observed as a consequence of cooperative phase interaction, for example.<sup>[7,9]</sup> The use of spatially-resolved and phase selective analytical techniques therefore becomes increasingly relevant in order to accurately address the catalyst structure.<sup>[19–21]</sup> For example, common techniques such as laboratory powder X-ray diffraction (PXRD) or synchrotron radiation-based X-ray absorption spectroscopy (XAS) can reveal valuable information on crystalline and amorphous phases, including active site properties such as metal oxidation state and coordination environment. However, conventional bulk measurements on powders or packed beds result in averaged data, which may lack the sensitivity needed to identify dilute or minority species present, particularly in quaternary MMO catalysts. Ideally, a complete knowledge of all phases is the ultimate goal to allow full understanding and rationalisation of both catalytic performance and the phases contributing to this. No single analytical technique can solve this problem, rather the careful application of cooperative techniques is required.

In this work, we applied a range of advanced spatially-resolved chemical imaging methods for characterisation of MMO catalysts across multiple length-scales. A highly active quaternary Bi–Mo–Co–Fe oxide catalyst for selective propylene oxidation to acrolein was taken as a case study. The chemical imaging approach is demonstrated starting with scanning electron microscopy (SEM) and Raman spectroscopic mapping for 2D phase characterisation of metal oxide species over extended regions of powder samples.<sup>[22–23]</sup> Moving beyond 2D composition towards entire single catalyst particles, we employed a combination of hard X-ray fluorescence nanotomography (XRF-CT) and phase contrast holotomography to observe

the distribution of each elemental component in 3D within the particle ensemble. Furthermore, the complex crystalline phase structure was partially deconvoluted within a single catalyst particle using hard X-ray diffraction microtomography (XRD-CT), which can non-invasively identify and locate individual phase contributions in 3D space.<sup>[24–28]</sup> To highlight the power of these advanced 3D techniques, we compare them to global characterisation of the MMO catalyst after reaction by PXRD, XAS and Raman spectroscopy, which could isolate relatively few structural components. By using such modern spatially-resolved characterisation tools, we can re-evaluate long-standing MMO particle models, such as olefin oxidation over Bi–Mo–Co–Fe oxide catalysts, which can be refined in future using the chemical imaging approach shown here.

## Results and Discussion

### Catalytic tests

A quaternary Bi–Mo–Co–Fe oxide catalyst (9/52/29/11 mol%) was prepared by a hydrothermal synthesis method reported previously.<sup>[18]</sup> It represents a modern complex-structured MMO catalyst and serves as a model system to those used in industry. The hydrothermally-prepared Bi–Mo–Co–Fe oxide catalyst was tested for its catalytic performance in propylene oxidation. For comparison, phase pure  $\alpha\text{-Bi}_2\text{Mo}_3\text{O}_{12}$  prepared by hydrothermal synthesis (HS), and a Bi–Mo–Co–Fe oxide reference catalyst prepared by co-precipitation (CP), were also tested. The specific surface area was measured for each catalyst after synthesis and calcination but prior to catalytic testing, with values of  $5\text{ m}^2\text{ g}^{-1}$  (2-component Bi–Mo, HS),  $7\text{ m}^2\text{ g}^{-1}$  (4-component Bi–Mo–Co–Fe oxide, CP), and  $19\text{ m}^2\text{ g}^{-1}$  (4-component Bi–Mo–Co–Fe oxide, HS) obtained. The results of catalytic testing are shown in Figure 1.

For feed streams from 27.1 to 81.3  $\text{mmol}_{\text{propylene}}\text{ g}_{\text{catalyst}}^{-1}\text{ h}^{-1}$  (weight hourly space velocity ( $\text{WHSV}_{\text{C}_3\text{H}_6}$ ) ranging from 0.57 to  $3.42\text{ h}^{-1}$ ), the hydrothermally-synthesised Bi–Mo–Co–Fe oxide catalyst was best performing. For instance, at  $\text{WHSV}_{\text{C}_3\text{H}_6} = 1.14\text{ h}^{-1}$ , 63% propylene conversion and 76% acrolein selectivity were obtained. Under the same conditions, pure  $\alpha\text{-Bi}_2\text{Mo}_3\text{O}_{12}$  showed 22% conversion and 89% acrolein selectivity and the co-precipitated Bi–Mo–Co–Fe oxide catalyst showed 54% conversion at 63% selectivity. Furthermore, the presented multicomponent catalyst showed a higher acrolein selectivity at similar propylene conversions. At around 39–45% propylene conversion, the selectivity increased in the order of: CP: Bi–Mo–Co–Fe oxide (64% at  $1.71\text{ h}^{-1}$ ) < HS:  $\alpha\text{-Bi}_2\text{Mo}_3\text{O}_{12}$  (74% at  $0.57\text{ h}^{-1}$ ) < HS: Bi–Mo–Co–Fe oxide (80% at  $2.28\text{ h}^{-1}$ ). In general, the acrolein selectivity increased with higher  $\text{WHSVs}$ . The main by-products observed were CO and  $\text{CO}_2$ , whereas the co-precipitated Bi–Mo–Co–Fe oxide showed a high selectivity toward acrylic acid. The specific surface area of the 4-component hydrothermally-synthesised catalyst decreased to  $7\text{ m}^2\text{ g}^{-1}$  after catalytic testing, closely matching the initial values for the other catalysts. Overall, catalytic performance tests illustrate how activity and selectivity are strongly improved

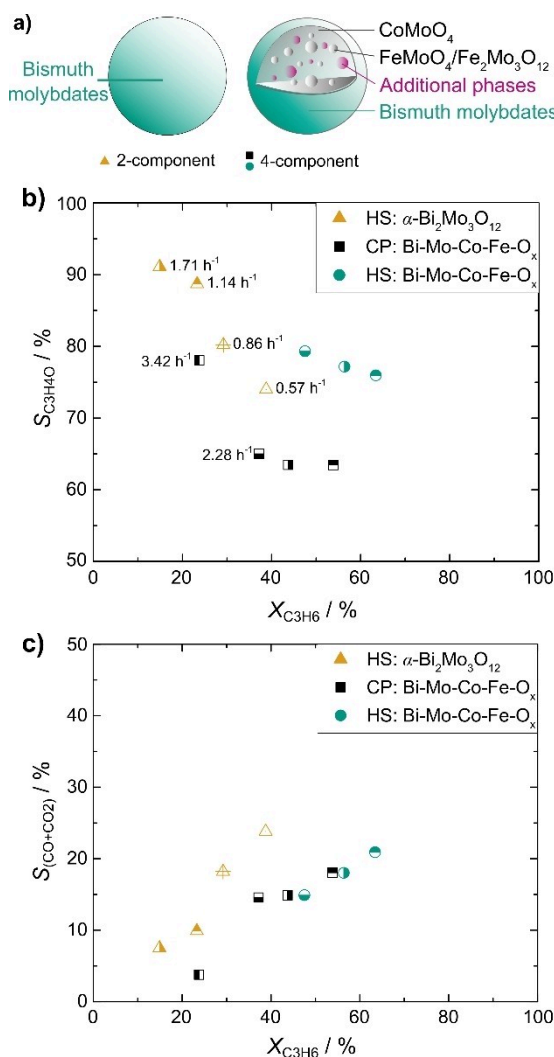


**Figure 1.** (a) Illustration of a simple binary particle and a complex quaternary Bi–Mo–Co–Fe oxide particle model according to Ref. [8–10]; (b) comparison of acrolein selectivity over propylene conversion at 380 °C; (c) comparison of combined CO and CO<sub>2</sub> selectivity over propylene conversion at 380 °C. CP = co-precipitation, HS = hydrothermal synthesis. Data point shading indicates WHSV<sub>C<sub>3</sub>H<sub>6</sub></sub> of the measurement.

for the quaternary Bi–Mo–Fe–Co oxide systems, which can be explained in principle by the cooperation of interacting phases. This includes phases which may not be present in simple binary or model systems. Furthermore, the performance clearly also depends on the synthetic history of the catalyst material. Due to the excellent performance of the hydrothermally-synthesised quaternary system, the specific phase composition and possible interactions were investigated further by both global and spatially-resolved techniques.

#### Global characterisation

Laboratory PXRD was performed to access the overall composition of crystalline phases, revealing in particular β-CoMoO<sub>4</sub>, Co<sub>0.7</sub>Fe<sub>0.3</sub>MoO<sub>4</sub>, α-Bi<sub>2</sub>Mo<sub>3</sub>O<sub>12</sub> and γ-Bi<sub>2</sub>MoO<sub>6</sub> as major compo-

nents. Based on the PXRD pattern acquired after catalytic testing shown in Figure 2, it was not possible to distinguish between Bi/Mo/Fe or Fe/Mo phases such as Bi<sub>3</sub>FeMo<sub>2</sub>O<sub>12</sub> (the former indicated by SEM-EDX, Figure 3) due to overlapping reflections. In general, the PXRD reflections both before (see ESI) and after testing were highly convoluted and accurate phase assignment of such complex ensembles was therefore challenging. Quantitative crystalline phase analysis can in principle be achieved via Rietveld refinement, but is challenging on a complex mixture of up to four components with an unknown total number of phases present. Furthermore, PXRD is only sensitive to crystalline phases, while MMO catalysts may also contain amorphous or disordered features, which require complementary characterisation by XAS or Raman spectroscopy, for example.

In the current study, XAS was performed on pellets of the quaternary hydrothermally-synthesised catalyst after reaction (see results in ESI). Analysis indicated the presence of species including α-Bi<sub>2</sub>Mo<sub>3</sub>O<sub>12</sub> and γ-Bi<sub>2</sub>MoO<sub>6</sub> (based on Mo K edge and Bi L<sub>3</sub> edge) in agreement with PXRD, and α-CoMoO<sub>4</sub> (based on Co K edge). For conventional PXRD, Raman spectroscopy and XAS however, the challenge of distinguishing major and minor phases depends on the focal spot size of the beam relative to the separation or distribution of microstructural features in the

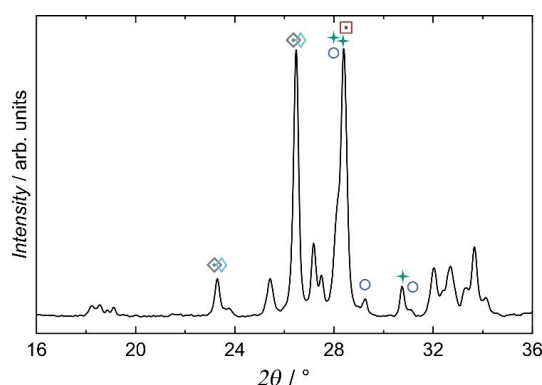


**Figure 2.** PXRD pattern of the hydrothermally-synthesised catalyst after catalytic tests. Assigned phases: ○ α-Bi<sub>2</sub>Mo<sub>3</sub>O<sub>12</sub> (ICSD: 2650), □ γ-Bi<sub>2</sub>MoO<sub>6</sub> (ICSD: 47139), ◇ β-CoMoO<sub>4</sub> (JCPDS no. 21–868), ◇ Co<sub>0.7</sub>Fe<sub>0.3</sub>MoO<sub>4</sub> (ICSD: 280035) and + Bi<sub>3</sub>FeMo<sub>2</sub>O<sub>12</sub> (ICSD: 45).

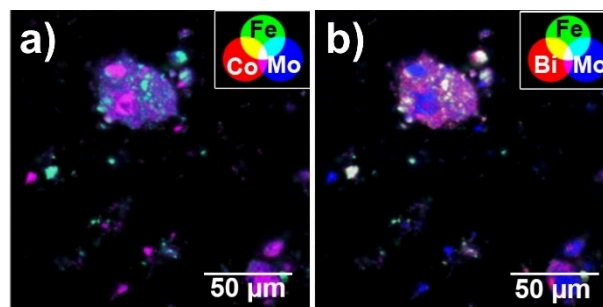


**Figure 3.** SEM-EDX images of hydrothermally-synthesised Bi–Mo–Co–Fe oxide catalyst after testing with colour coding for individual metals, and the overlap between: (a) Fe, Co, Mo; (b) Fe, Bi, Mo.

material. Due to the averaging nature of the measurements in this case, they are not sufficiently sensitive to minor phases. A spatially-resolved approach in 2D or 3D is necessary to avoid convoluted or superimposed spectra of different metal oxide components which may be difficult to isolate.

### SEM-EDX mapping

To illustrate the heterogeneity of the hydrothermally-synthesised catalyst, SEM-EDX mapping was performed after catalytic testing. As shown in Figure 3, larger irregular shaped particles were found intermixed with sub-micrometre-sized and well-defined crystals. Area mapping with SEM-EDX gave access to the elemental distribution, revealing agglomerates of mainly binary Bi–Mo oxide as expected, but additionally clear indications of mixed binary Co–Mo oxide and ternary Bi–Mo–Fe oxide species. Notably, the larger homogeneous areas coincided with Co–Mo oxide agglomerates, with several smaller areas associated with Bi–Mo–Fe oxides. However, while SEM-EDX mapping is useful in determining elemental distribution, it is not sensitive to the phase composition of the sample (e.g., bismuth molybdate morphology present in Bi–Mo oxide areas). In principle, the phase composition can be studied with selected area electron diffraction (SAED), but this is only suitable for analysing local composition in a small area with potentially invasive sample preparation. For the same reason, transmission electron microscopy (TEM) also has limited practical use in this case due to observed heterogeneity on the micrometre scale and the highly localised nature of the images which can be acquired. For more complete phase identification of MMO catalysts in their native form as microscale particles, alternative spatially-resolved techniques such as 2D Raman spectroscopy are required.

### Spatially-resolved Raman spectroscopy and 2D mapping

By employing a focused laser beam, Raman spectroscopy is especially suited for spatially-resolved 2D sample mapping and is additionally sensitive to both crystalline and amorphous phases. Here Raman mapping was performed on the hydrothermally-synthesised quaternary Bi–Mo–Co–Fe oxide catalyst after testing by raster-scanning a focused beam over the surface of the catalyst sample (532 nm laser, laser spot size: 0.38  $\mu\text{m}$ , area  $56 \times 56 \mu\text{m}^2$ , 0.2  $\mu\text{m}$  raster step size; Figure 4a). For each of the 78,400 single spectra recorded, a direct classical least squares (DCLS) component analysis was performed using reference spectra including pure  $\alpha\text{-Bi}_2\text{Mo}_3\text{O}_{12}$ ,  $\beta\text{-Bi}_2\text{Mo}_2\text{O}_9$ ,  $\gamma\text{-Bi}_2\text{Mo}_2\text{O}_6$ ,  $\alpha\text{-CoMoO}_4$ ,  $\beta\text{-CoMoO}_4$ ,  $\beta\text{-FeMoO}_4$ ,  $\text{Fe}_2\text{Mo}_3\text{O}_{12}$ ,  $\text{Bi}_3\text{FeMo}_2\text{O}_{12}$  and  $\text{MoO}_3$  (Figure 4c–h, not all references are shown).

Notably, the phase distribution observed was quite heterogeneous. Numerous overlapping regions of  $\alpha\text{-Bi}_2\text{Mo}_3\text{O}_{12}$  (dark blue spectrum) and  $\gamma\text{-Bi}_2\text{Mo}_2\text{O}_6$  (red spectrum) were observed as larger well-distributed agglomerates (Figure 4c,e). This can also be observed in the spectrum extracted from ROI 3 for example,

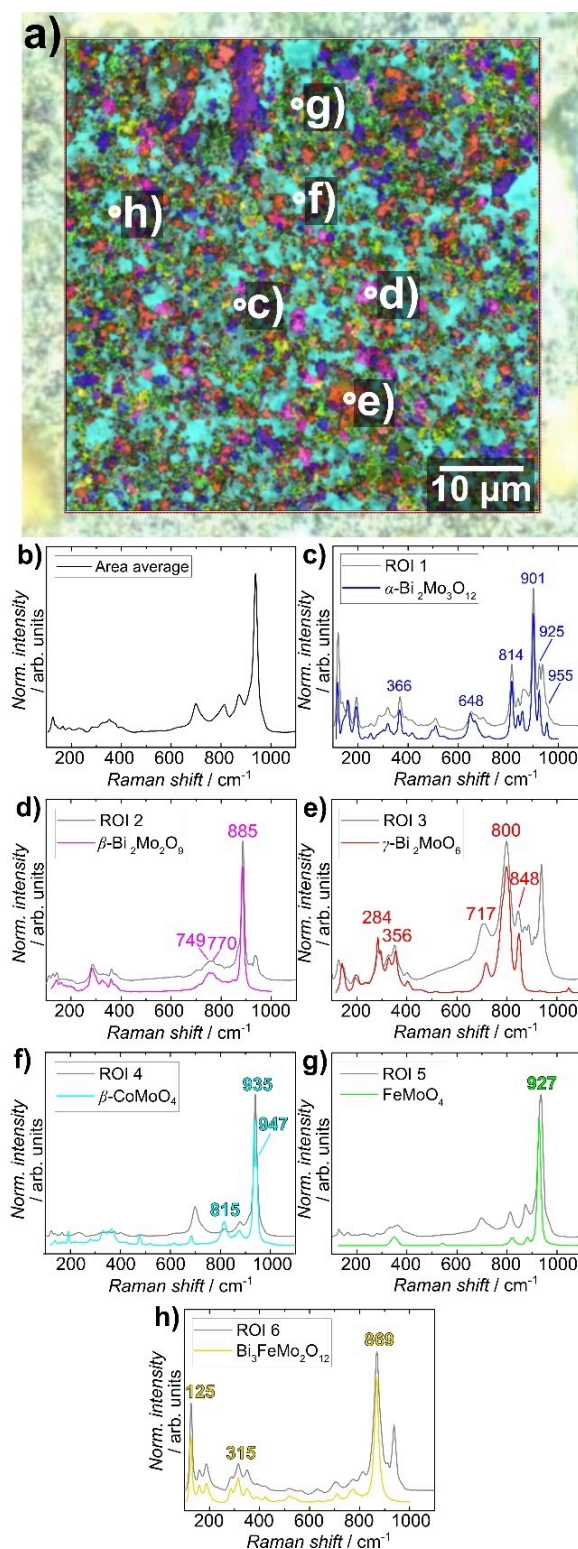


**Figure 4.** (a) 2D Raman spectroscopic phase distribution obtained from DCLS-based component analysis and plotted over the optical microscopic image of HS: Bi–Mo–Co–Fe oxide after testing. (b) Averaged Raman spectrum for the whole area, and spectra extracted from regions of interest, which were colour-coded assigned to certain phases based on DCLS component analysis: (c)  $\alpha\text{-Bi}_2\text{Mo}_3\text{O}_{12}$  (blue), (d)  $\beta\text{-Bi}_2\text{Mo}_2\text{O}_9$  (magenta), (e)  $\gamma\text{-Bi}_2\text{Mo}_2\text{O}_6$  (red), (f)  $\alpha/\beta\text{-CoMoO}_4$  (cyan), (g)  $\text{FeMoO}_4$  (green), (h)  $\text{Bi}_3\text{FeMo}_2\text{O}_{12}$  (yellow).



where in addition to main features from the  $\gamma$ - $\text{Bi}_2\text{MoO}_6$  reference, additional bands at  $901\text{ cm}^{-1}$  ( $\alpha$ - $\text{Bi}_2\text{Mo}_3\text{O}_{12}$ ) and  $935\text{ cm}^{-1}$  ( $\beta$ - $\text{CoMoO}_4$ ) are clearly visible. This indicates an intermixing of the above phases. On the other hand,  $\beta$ - $\text{Bi}_2\text{Mo}_2\text{O}_9$  (pink spectrum) appeared mainly in isolated domains, indicated by the good match of the relevant reference with the ROI 2 spectrum (Figure 4d). However, the  $\beta$ - $\text{Bi}_2\text{Mo}_2\text{O}_9$  content was low and it was neither detected by PXRD, nor in averaged Raman spectra of the scanned area, due to overshadowing or convolution with more intense neighbouring bands. The main visible component was  $\alpha/\beta$ - $\text{CoMoO}_4$  (light blue spectrum), as evident from the average spectrum (Figure 4b) and the large proportion of matching coloured areas in Figure 4a. It is uncertain whether this phase was particularly highly concentrated, or whether it could essentially not be resolved from neighbouring phases due to the spatial resolution of the measurement (see ESI).  $\text{FeMoO}_4$  (green spectrum) was occasionally present in smaller particles and highly dispersed, compared to the Co and Bi molybdate phases mentioned previously. A  $\text{Bi}_3\text{FeMo}_2\text{O}_{12}$  mixed phase (yellow spectrum) was also found in the form of randomly dispersed micrometre-sized particles, indicated by the good match between the reference spectrum and ROI 6 (Figure 4h). This is in agreement with the presence of Bi/Mo/Fe domains found via SEM-EDX. However, no Raman bands corresponding to  $\text{Fe}_2\text{Mo}_3\text{O}_{12}$  and  $\text{MoO}_3$  were found.

The apparent low amount of binary  $\text{Fe}_2\text{Mo}_3\text{O}_{12}$  phases by both Raman mapping and SEM-EDX on the microscale is significant, as it implies incorporation of iron into a ternary Bi–Mo–Fe oxide form, which has been linked to improved acrolein selectivity as observed here.<sup>[11,29–30]</sup> While limited amounts of  $\text{MoO}_3$  were suggested to be beneficial for the catalyst in terms of replenishing reduced oxide species, excess  $\text{MoO}_3$  has been linked with decreased activity for propylene oxidation. This was particularly observed for catalysts with relatively higher Mo content.<sup>[9,31]</sup> The absence of any visible isolated  $\text{MoO}_3$  species here is also in agreement with the generally high catalytic performance.

For proper data interpretation, the limitations of Raman spectroscopy must be considered. Since inelastic Raman scattering is generally a weak effect, quantification is not easily achievable especially for minority phases or those with weak Raman bands. The absence of some phases in the measured Raman spectrum might originate from low scattering intensity, even though spatially resolved acquisition was performed. In addition, the resolution of  $>0.38\text{ }\mu\text{m}$  obtained here (see ESI) is mainly restricted by the diffraction limit of visible light ( $532\text{ nm}$ ,  $100\times$  objective,  $\text{NA}=0.85$ ), and might not be high enough to resolve neighbouring phases completely. Furthermore, phase pure references are needed for DCLS analysis, which is challenging and time consuming in the absence of standard databases for Raman spectroscopy, such as those which exist for XRD data. While the resolution can be increased using methods like tip enhanced Raman spectroscopy (TERS),<sup>[32–33]</sup> this may not be suitable for representative imaging of large samples used in heterogeneous catalysis.

A clear distinction should be made between investigation of simple binary Bi–Mo oxide systems, for which Raman spectro-

scopy mapping may be sufficient to address the structure, and the much more complex quaternary Bi–Mo–Co–Fe oxide systems. In addition, the limitations of 2D mapping over a region of the catalyst surface (according to the penetration depth), compared to examination of larger bulk particles should also be considered. For effective chemical imaging at higher spatial resolution on larger samples, it is therefore necessary to consider hard X-rays as the more suitable probe.

### X-ray holotomography and XRF-CT

The highly brilliant hard X-rays produced by modern synchrotron light sources offer excellent opportunities for catalyst characterisation by means of chemical imaging in 2D and 3D. In particular, hard X-ray tomography offers high penetration depth for measuring samples with larger diameter, compared to optical or electron microscopy. The acquisition of 3D spatially-resolved data using tomography is therefore feasible on large samples, which allows for deconvolution of internal structural features. A range of contrast modes are also available based on the interactions of hard X-rays with matter. Here, a single particle of the hydrothermally-synthesised quaternary Bi–Mo–Co–Fe oxide catalyst after catalytic testing was studied at beamline ID16B of the European Synchrotron Radiation Facility (ESRF), first using full-field phase contrast holotomography, followed by nanofocused XRF-CT, with beam attenuation measured simultaneously by tomographic scanning transmission X-ray microscopy (STXM-CT).

Phase contrast holotomography produced a macroscopic view of the entire catalyst particle with around  $25\text{ nm}$  voxel size and an assumed resolution of  $>100\text{ nm}$  (Figure 5a), allowing analysis of structurally diverse regions based on their relative electron density. Three representative slices of the catalyst particle are shown, from which needle or plate-like structures were observed (Figure 5b). Comparing the holotomogram to the sample attenuation measured at the same position by STXM-CT (Figure 5c) supported the presence of highly absorbing components attributed to metal oxides, together with regions of low attenuation (see ESI, possibly from carbon deposits or glue which was not fully segmented during visualisation). A non-discriminating imaging method such as holotomography or STXM-CT is therefore highly useful for visualising global sample structure regardless of composition, although these methods cannot directly identify features contributing to differing contrast regions.

Consequently, XRF-CT was applied to isolate individual signals of Bi, Mo, Co and Fe within the catalyst particle (Figure 5d). The needle or plate-shaped structures observed by holotomography were thus composed mainly of Mo, in addition to contributions of Bi. This is consistent with previous studies.<sup>[34]</sup> However, while Mo was distributed rather homogeneously throughout the entire sample, Co and Fe were often observed as a pair and were mostly segregated from the other metals (see overlay images in ESI). This indicates that phases composed of at least two components (Bi and Mo) formed larger or more extended structures, while Co and Fe may have formed in a

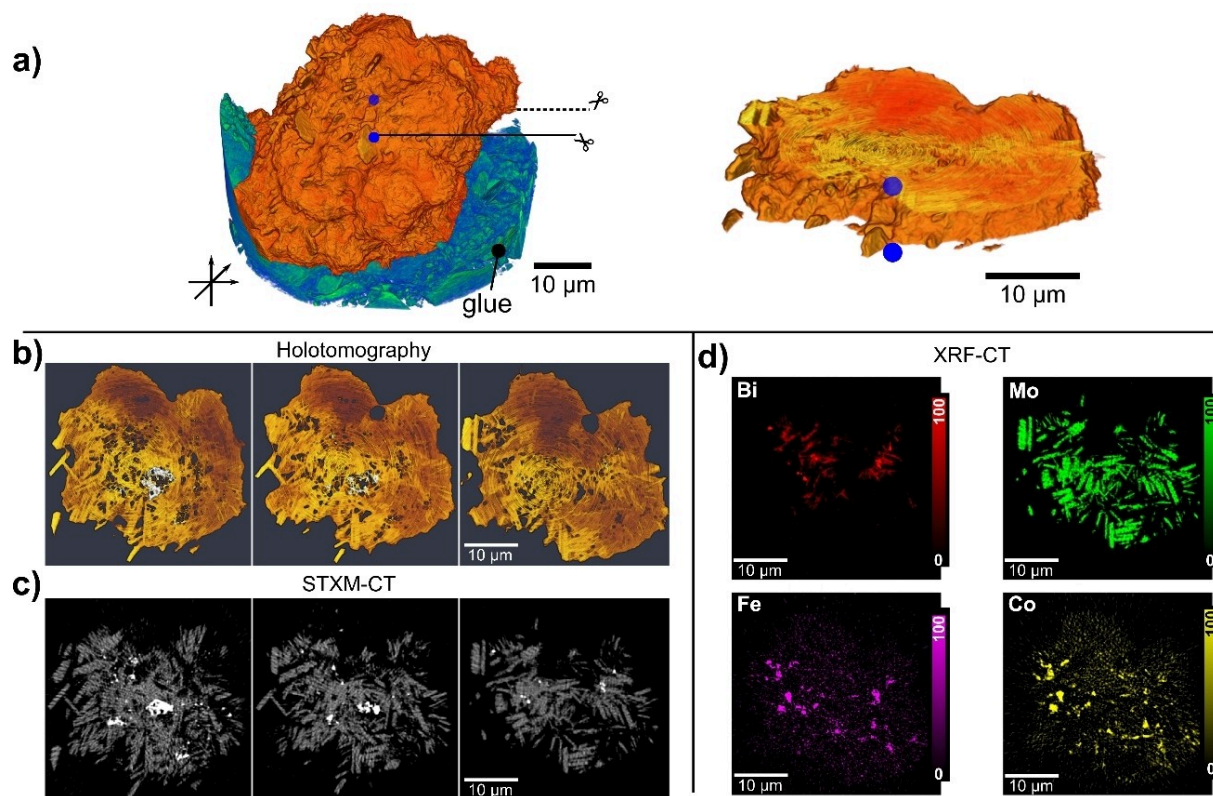


**Figure 5.** (a) Holotomography visualisation of the entire HS: Bi–Mo–Co–Fe oxide particle following catalytic tests, with the sample glued to the top of a tomography pin; identical orthogonal slices extracted from the tomographic volume showing individual signals obtained from (b) holotomography; (c) STXM-CT; and (d) normalised XRF-CT showing absolute intensity (signal including 0–100% of histogram values) of each metal component.

more particulate or agglomerated manner around these structures, in agreement with observations in the literature.<sup>[11]</sup> Notably, Co and Fe species often overlapped, occasionally also with Bi (see ESI). Due to the relatively high global composition of Mo observed, this probably also indicates the presence of some Co–Fe–Mo oxide species. This may partly explain the relatively high selectivity towards acrolein, since the presence of mixed Co–Fe molybdates was shown to be beneficial in this regard compared to individual  $\text{CoMoO}_4$  or  $\text{FeMoO}_4$  phases.<sup>[11]</sup> Compared to SEM-EDX (Figure 3), XRF-CT has the benefit of non-invasively probing the metal speciation within entire catalyst particles. However, it should be noted with caution that Co and Fe have relatively low fluorescence signal due to the high incident X-ray energy applied (29.6 keV). In addition, there is strong potential for self-absorption artefacts from the relatively low energy of Co- $K_{\alpha}$  and Fe- $K_{\alpha}$  emission lines combined with high concentration of these elements in a relatively thick sample. In addition, none of the above methods are sensitive to specific crystalline phase, therefore the exact same particle was further investigated by XRD-CT.

### XRD-CT

XRD-CT was performed on a single particle of the hydrothermally-synthesised quaternary Bi–Mo–Co–Fe oxide catalyst

after testing. Crystalline phases within the entire particle were measured with a beam spot size of around 650 nm. This allowed us to deconvolute the diffraction patterns and identify local phases within the catalyst particle, which is not possible using conventional PXRD either in the laboratory or at the synchrotron. Figure 6 shows diffractograms of selected regions of interest (ROI 1–3) which revealed a heterogeneous phase distribution across different regions of the catalyst particle, compared to the average diffractogram of one complete slice of the catalyst particle (Sum ROI – representative of a ‘typical’ PXRD pattern as shown in Figure 2). At the same time, the relatively non-linear background shown in the average diffraction pattern further suggests some contribution of amorphous species, although these cannot be identified with XRD. While many crystalline features were still convoluted, based on available reference patterns it was possible to partly assign and isolate several individual phases (Figure 6), including:  $\beta\text{-Co}_{0.7}\text{Fe}_{0.3}\text{MoO}_4/\beta\text{-CoMoO}_4$  ( $2\theta = 10.06/10.07^\circ$ ),  $\alpha\text{-Bi}_2\text{Mo}_3\text{O}_{12}$  ( $11.04^\circ$ ) and  $\text{Bi}_3\text{FeMo}_2\text{O}_{12}$  ( $7.04^\circ$ ). Note that the features at  $2\theta = 10.06/10.07^\circ$  cannot be distinguished from each other, and are therefore given an ambiguous label to indicate the presence of either phase, or both phases. It was furthermore possible to present the distribution of these isolated phases within the particle, revealing a relatively homogeneous distribution of  $\beta\text{-Co}_{0.7}\text{Fe}_{0.3}\text{MoO}_4/\beta\text{-CoMoO}_4$ , also indicated by the strong feature at  $10.06^\circ$  in the Sum ROI (Figure 6a). Several closely overlapping

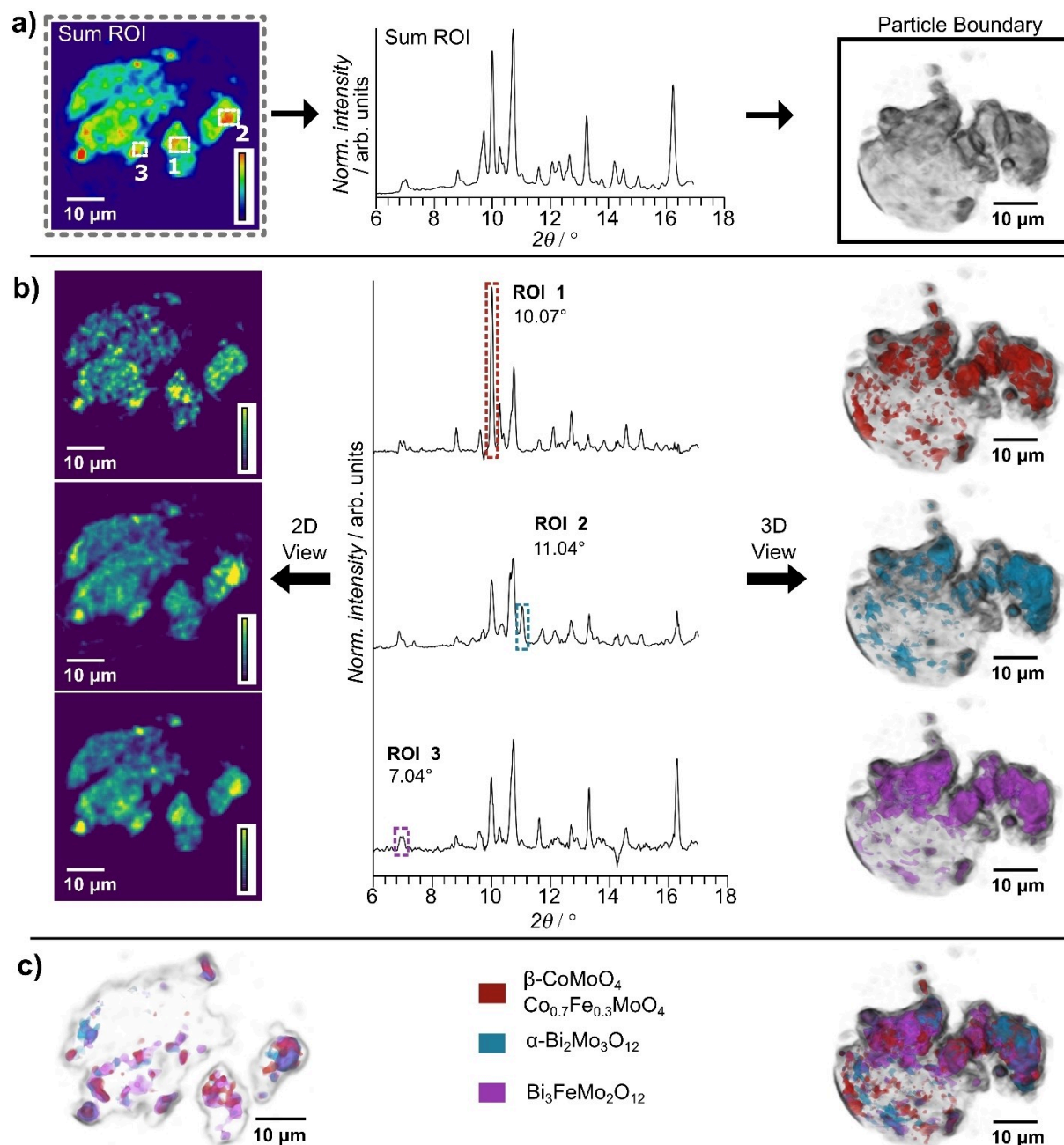


**Figure 6.** XRD tomography of a single catalyst particle after reaction: (a) spatially-resolved XRD patterns of selected areas (ROI 1–3) and summed ROI of all pixels in an entire slice (Sum ROI) – the particle boundary is illustrated by a transparent rendering; (b) integral of selected reflections (highlights at  $10.07^\circ$ ,  $11.04^\circ$ ,  $7.04^\circ$ ) from the XRD patterns acquired in ROI 1–3 – the slices on the left indicate the normalised individual pixel intensity of the selected reflection in 2D space, the volumes on the right show the pixels with top 15% measured intensity across all slices in 3D space; (c) illustration of the overlap between selected reflections presented as a single orthographic slice through the 3D rendered volume (left) and the entire 3D volume (right). The selected reflections shown contain  $2\theta$  values characteristic of  $\beta$ -CoMoO<sub>4</sub>/Co<sub>0.7</sub>Fe<sub>0.3</sub>MoO<sub>4</sub> ( $10.07^\circ$ ),  $\alpha$ -Bi<sub>2</sub>Mo<sub>3</sub>O<sub>12</sub> ( $11.04^\circ$ ) and Bi<sub>3</sub>FeMo<sub>2</sub>O<sub>12</sub> ( $7.04^\circ$ ) as well as the overlap of all three phases ( $\lambda = 0.05904$  nm).

but heterogeneously dispersed regions of  $\alpha$ -Bi<sub>2</sub>Mo<sub>3</sub>O<sub>12</sub> ( $11.04^\circ$ ) and Bi<sub>3</sub>FeMo<sub>2</sub>O<sub>12</sub> ( $7.04^\circ$ ), indicated by overlap of the intense regions of these features in Figure 6b. This strongly supports the results observed by 2D Raman spectroscopic mapping of catalyst powder surfaces (Figure 4) and XRF nanotomography imaging of the entire catalyst particle (Figure 5), whereby Fe and Co species were found to agglomerate, and Bi<sub>3</sub>FeMo<sub>2</sub>O<sub>12</sub>

was present together with binary bismuth molybdate phases. The strong overlap of binary Bi–Mo oxide and ternary Bi–Mo–Fe oxide phases observed at the particle scale is consistent with the concept of phase cooperation in selective oxidation catalysis described by Grasselli.<sup>[35]</sup> In combination with the overlapping binary Co–Mo oxide or ternary Co–Fe–Mo oxide observed, these results may partly explain the superior catalytic

performance observed in propylene oxidation for the quaternary compared to the binary system.<sup>[36]</sup> Due to overlap between neighbouring features, it was not possible to conclusively isolate more individual phase contributions from the XRD-CT data obtained in this instance. We further emphasise that without use of spatially-resolved techniques such as XRD-CT, it would be challenging or even impossible to conclusively identify close mixtures of phases with similar diffraction patterns (see references in ESI). At the same time, due to the apparent high heterogeneity across single particles of Bi–Mo–Co–Fe oxide shown here, localised probes such as TEM or SAED risk being unrepresentative of catalyst composition at the particle scale. This demonstrates the importance of analysing the complex phase structure of such catalysts by spatially-resolved methods capable of probing at the particle scale. Although hindered in this case by the high complexity of the sample, XRD-CT still demonstrates the capability to define the spatial distribution of crystalline phases in 3D-space. Thus, it is possible to produce a physical visualisation of the simple particle model, even considering more complex by-phases. Nevertheless, XRD-CT is still limited to observation of crystalline structure, therefore in future it may be advantageous to consider tomographic XAS, total scattering or pair distribution function analysis, which offer the necessary sensitivity regardless of the presence of crystalline or amorphous components.<sup>[37]</sup> In the case of MMOs for selective propylene oxidation most phases are probably crystalline, but this does not exclude formation of non-crystalline features at surfaces or particle interfaces. The results show the excellent potential of tomographic data compared to global analysis such as conventional PXRD. It is of considerable interest in the future to further address the structure of complex heterogeneous catalytic systems such as MMOs using tomography.

### Structural insights from spatially-resolved analysis

A multiphase system of quaternary Bi–Mo–Co–Fe oxide prepared by hydrothermal synthesis was studied as highly active and selective catalyst for propylene oxidation to acrolein. The performance of the quaternary catalyst was shown to exceed that of a binary Bi–Mo oxide system. The structural complexity of this quaternary MMO catalyst is difficult to analyse by global characterisation methods, therefore making it an excellent representative case study for demonstrating the importance and application of emerging spatially-resolved analytical techniques in catalysis.

This work demonstrates that all the necessary tools are in place for systematic investigation of complex quaternary MMO catalysts. Indeed, a combined characterisation approach may be necessary to conclusively identify interactions and synergy between specific phases. Global methods including Raman spectroscopy, PXRD and XAS are unable to address the catalyst complexity in a sufficient manner. Therefore, a systematic assessment was performed using 2D spatially-resolved SEM-EDX and Raman spectroscopy mapping, and 3D spatially-resolved X-ray micro- and nanotomography. SEM-EDX mapping gave an

overview over the heterogeneous metal distribution and clustering of certain elements. With 2D Raman spectroscopic mapping, phase identification and distribution of both crystalline and amorphous phases on a sub-micrometre resolution was monitored, allowing identification of by-phases that were masked during previous analysis with global characterisation methods. Deconvolution of Raman data by DCLS-based analysis allowed a deeper insight into the catalyst composition. This makes Raman spectroscopy especially suitable for complex MMOs, but notably depending on whether appropriate reference materials are available for DCLS.<sup>[38]</sup> In general, for MMOs that are intermixed on the micrometre-scale, Raman mapping offers a convenient resolution. Large scanning areas can be sampled with modern Raman spectrometers on a reasonable timescale (ca. 2 d). Combined with the latest *operando* cells, MMO mapping is even possible during catalytic reactions.<sup>[39–40]</sup> Nevertheless, Raman spectroscopy has a limited material sensitivity due to the weak scattering signal, and additionally a limited information-depth due to high attenuation of optical wavelengths including near-UV, visible, and near-IR regions. While Raman spectroscopic mapping can be applied with 3D spatial resolution (e.g., confocal microscopy),<sup>[41]</sup> this has typically been limited to micron sized samples at most, and it is difficult to imagine this applied to larger catalyst particles on the order of > 50  $\mu\text{m}$  as studied here. In comparison, hard X-ray tomography allows non-invasive analysis of large particles with a range of contrast modes, including absorption, X-ray fluorescence, diffraction and phase as demonstrated in this case study. For the presented catalyst, crystalline phases and their agglomeration and, thus, cooperation, was visualised for a spent catalyst particle in 3D-space via XRD-CT. The crystalline phases were identified by a relatively simple approach of assigning specific individual reflections from known references, but XRD analysis and phase mapping can be extended by Rietveld refinement as demonstrated elsewhere.<sup>[27,42]</sup> Notably, this approach is most successful when powder diffraction conditions can be maintained during tomography acquisition, and single crystal artefacts and preferred orientation of larger crystallites are minimised. Despite the high complexity of four-component catalysts, the information derived in this study strongly complements the presently oversimplified binary MMO systems ( $\alpha$ -,  $\beta$ -,  $\gamma$ -bismuth molybdates). Nevertheless, this increased complexity and the presence of additional metal oxide phases is directly responsible for the superior activity of quaternary systems. Only through a careful characterisation approach can the necessary information be extracted to further develop and improve on well-known particle models which are still in use today. In particular, while the current study presents only *ex situ* characterisation, it is also crucial to consider spectroscopic and tomographic measurements under *in situ* conditions, which have the potential to track changes in the catalyst structure and activity as a function of chemical environment.<sup>[43]</sup>



## Conclusion

By exploiting the synergy between spatially-resolved techniques, it was possible to advance from a simplified particle model of interacting phases, to empirical 2D and 3D images of the catalyst particle with identification of several main- and by-phases. A clear distinction can be made between model or binary systems which are less structurally diverse, and the complex quaternary systems investigated here. The latter case requires the use of advanced spatially-resolved characterisation tools to aid in making meaningful observations on the catalyst structure. The strong activity of the catalyst for selective oxidation of propylene can be rationalised in part by: (i) the presence of mixed ternary metal oxide phases including Bi–Mo–Fe oxide and Co–Fe–Mo oxide in addition to binary Bi–Mo oxide; (ii) the absence of isolated  $\text{MoO}_3$ , which in excess is known to hinder catalytic activity. These observations are challenging without the use of complementary characterisation tools sensitive to different elements, crystalline and amorphous phases, and capable of deconvolution and colocation in 2D and 3D space. Future studies should aim to provide a complete characterisation of the MMO structure by means of better spatial- or energy-resolution during XRD-CT or alternative methods, such as XANES-CT for individual mapping of metal oxidation states and coordination environment, or PDF-CT and total scattering for high quality analysis of nanostructured phases. A modern spatially-resolved characterisation approach must demonstrably consider multiple length scales, detection methods and sample sizes, in order to unlock new information about complex MMO systems. Strategies for handling and evaluating the large quantities of data produced by such detailed characterisation tools are an essential concern which must be strongly in focus moving forward.

## Experimental Section

### Catalyst preparation

The four-component catalyst system (HS: Bi–Mo–Co–Fe oxide) was prepared by hydrothermal synthesis according to a recently established procedure.<sup>[18]</sup> The calculated precursor ratio is listed in Table S1 (see ESI). The precursor  $(\text{NH}_4)_6\text{Mo}_7\text{O}_{24} \cdot 4\text{H}_2\text{O}$  was solubilised in 20 mL distilled water and stirred for 15 min. In parallel, a solution consisting of  $\text{Bi}(\text{NO}_3)_3 \cdot 5\text{H}_2\text{O}$ ,  $\text{Co}(\text{NO}_3)_2 \cdot 6\text{H}_2\text{O}$  and  $\text{Fe}(\text{NO}_3)_3 \cdot 9\text{H}_2\text{O}$  in 20 mL  $\text{HNO}_3$  (2 M) was prepared and stirred for 15 min. Both solutions were combined in a Teflon® inlay and the pH was adjusted (pH=7) by adding dropwise an aqueous  $\text{NH}_3$  solution (25%) under continuous stirring. After additional stirring for 15 min, the inlay was transferred to a stainless-steel autoclave. The autoclave was heated to 180 °C for 24 h and afterwards allowed to cool down to RT (24 h). The obtained solid was filtered off (G4 glass frit) and washed three times with 10 mL  $\text{H}_2\text{O}$  and three times with 10 mL acetone. Finally, the catalyst was dried for 48 h at room temperature and subsequently calcined for 5 h at 320 °C. The preparation of the two-component catalyst system HS:  $\alpha\text{-Bi}_2\text{Mo}_3\text{O}_{12}$  is described elsewhere.<sup>[44]</sup>

### Catalytic performance tests

The setup for evaluation of the catalytic performance is described in detail in the literature.<sup>[44]</sup> The hydrothermally-prepared and subsequently calcined catalyst HS: Bi–Mo–Co–Fe oxide was ground, pressed and sieved to give a fraction of 300–450  $\mu\text{m}$ . 800 mg of the catalyst were placed in a quartz tubular reactor (6 mm inner diameter). For preconditioning in the setup, all catalysts were heated in synthetic air ( $\text{N}_2/\text{O}_2=80/20$ , 100  $\text{NmL min}^{-1}$ ) to 180 °C ( $5^\circ\text{C min}^{-1}$ ). Afterwards, sequential ramp steps to  $T_{1,\text{oven}}=345$ ,  $T_{2,\text{catalyst}}=380$ ,  $T_{3,\text{oven}}=380$ ,  $T_{4,\text{oven}}=400^\circ\text{C}$  ( $2^\circ\text{C min}^{-1}$ ) under reaction conditions ( $\text{N}_2/\text{O}_2/\text{C}_3\text{H}_6/\text{H}_2\text{O}=70/14/8/8$ ) with variation of total flow (100, 150, 200, 300  $\text{NmL min}^{-1}$ ) at each temperature were performed. Due to the exothermicity of the reaction, the oven temperature was regulated during testing to keep the catalyst bed temperature at 380 °C. The mass specific catalytic activity (MSCA) was calculated according to Equation (1). The weight hourly space velocity ( $\text{WHSV}_{\text{C}_3\text{H}_6}$ ) was calculated according to Equation (2) with  $\dot{V}$ : volume flow rate [ $\text{m}^3 \text{h}^{-1}$ ],  $\rho$ : density [ $\text{g m}^{-3}$ ],  $M$ : molar mass [ $\text{g mol}^{-1}$ ] and  $m$ : mass [ $\text{g}$ ]. Calculation of propylene conversion and acrolein selectivity can be found elsewhere.<sup>[44]</sup>

$$\text{MSCA} = \frac{\dot{V}_{\text{propylene}} \cdot \rho_{\text{propylene}}}{M_{\text{propylene}} \cdot m_{\text{catalyst}}} \quad (1)$$

$$\text{WHSV}_{\text{C}_3\text{H}_6} = \frac{\dot{V}_{\text{propylene}} \cdot \rho_{\text{propylene}}}{m_{\text{catalyst}}} \quad (2)$$

### Catalyst characterisation

The hydrothermally-prepared four-component catalyst (HS: Bi–Mo–Co–Fe oxide) was characterised by  $\text{N}_2$  physisorption, powder X-ray diffraction (PXRD), Raman spectroscopy, combined scanning electron microscopy and energy dispersive X-ray spectroscopy (SEM-EDX), inductively coupled plasma optical emission spectrometry (ICP-OES) and X-ray absorption spectroscopy (XAS). Characterisation results and additional information for the HS:  $\alpha\text{-Bi}_2\text{Mo}_3\text{O}_{12}$  catalyst can be found in the literature.<sup>[44]</sup> Where characterisation was performed after catalytic tests, this indicates the catalyst was removed from the reactor and characterised directly without any intermediate steps.

The specific surface area of the samples was measured by  $\text{N}_2$  physisorption at  $-196^\circ\text{C}$  using a BELSORP mini-II instrument (MicrotracBEL). Prior to the measurement, all samples were degassed in vacuum at 300 °C for 2 h. PXRD patterns were recorded on a Bruker D8 Advance diffractometer ( $\text{Cu K}_\alpha$  ( $\lambda=0.154 \text{ nm}$ ),  $\text{Ni-K}_\beta$  filter, Vantec PSD) in the  $2\theta$  range of 8 to 80° with a step size of  $0.0165^\circ$  and a dwell time of 2 s for each step. Phase assignment was performed using Inorganic Crystal Structure Database (ICSD) and Joint Committee of Powder Diffraction Standards (JCPDS) references. Raman spectroscopy was performed on a Renishaw inVia Reflex Raman Spectrometer using a frequency doubled Nd:YAG laser (532 nm, 100 mW at source) and a Leica optical microscope (100× objective). For 2D mapping an area of  $56 \times 56 \mu\text{m}^2$  was measured with a raster step size of 0.2  $\mu\text{m}$  and a laser spot size of 0.38  $\mu\text{m}$ . Spectra were recorded in the range of 60–1320  $\text{cm}^{-1}$  using a 2400 lines  $\text{mm}^{-1}$  grating with an acquisition time of 2 s. The laser intensity was set to 1%. SEM-EDX measurements were conducted using a JSM 7600F (JEOL) field-emission SEM at 20 kV, and an AZtec EDX system (Oxford Instruments). Samples were first embedded in epoxy glue and microtomed. The elemental metal composition was determined by ICP-OES using an Agilent 720/725-ES spectrometer. The sample was dissolved in 6 mL hydrochloric acid, 2 mL nitric acid and 1 mL hydrogen peroxide by using a microwave operated

at 600 W for 45 min. XPS measurements were performed using an ESCALAB 250 xi (ThermoFisher Scientific) equipped with an Al  $K_{\alpha}$  source at 1.487 keV, with a beam spot size of 900  $\mu\text{m}$  (results shown in ESI). X-ray absorption spectroscopy was performed at the ROCK beamline of the Soleil synchrotron (St. Aubin, France). Spectra of the catalyst sample after catalytic testing and of reference substances were obtained on pellets of the corresponding materials. For XAS data analysis the software package IFEFFIT<sup>[45]</sup> was used. For further information on XAS data treatment and results see ESI.

### X-ray tomography

The spent catalyst HS: Bi–Mo–Co–Fe oxide was investigated at the hard X-ray nanoimaging beamline ID16B of the European Synchrotron Radiation Facility (ESRF, Grenoble, France). Experimental details regarding: (i) full-field X-ray holotomography; (ii) scanning X-ray fluorescence nanotomography (XRF-CT); and (iii) scanning transmission X-ray tomography (STXM-CT) can be found in previous work.<sup>[46]</sup>

The exact same catalyst particle was further investigated at the hard X-ray microprobe endstation of beamline P06 at PETRA III (DESY, Hamburg, Germany). X-rays with an incident energy of 21 keV were focused to 650×500 nm (h×v) beam size using KB mirrors. Diffraction patterns were recorded at 50 ms exposure time using an Eiger X 4 M detector (Dectris; 2070×2167 pixels, pixel size of 75  $\mu\text{m}$ ) while raster scanning the sample with a horizontal step size of 0.4  $\mu\text{m}$ . The sample was scanned in a translate-rotate measurement scheme over 138 horizontal points (field of view 55.2×55.2  $\mu\text{m}^2$ ) and 180° rotation range (approx. 0.5° step size). The sample was then translated 0.5  $\mu\text{m}$  vertically and the acquisition procedure repeated to record a 3D volume consisting of approximately 50 slices. The calibration of the Debye-Scherrer rings was performed using  $\text{LaB}_6$  as a standard. Azimuthal integration of each sample point in the measured tomograms was performed using the pyFAI package<sup>[47]</sup> resulting in 660 individual 2 $\theta$  bins. Tomographic reconstruction was performed using maximum likelihood expectation maximisation (MLEM) algorithm.<sup>[48]</sup> Slice-by-slice analysis and extraction of regions of interest from the tomography volumes based on unique reflections was performed using DAWN.<sup>[49]</sup> Image normalisation, labelling, colour-mapping and 2D visualisation was performed using Fiji.<sup>[50]</sup> The Avizo 9.3 (Thermo Fisher Scientific) software package was used for 3D data visualisation. For further information on XRD data treatment and reference materials see ESI.

### Acknowledgements

We acknowledge DESY (Hamburg, Germany), a member of the Helmholtz Association HGF, for the provision of experimental facilities. Parts of this research (XRD-CT experiments) were carried out at beamline P06 (PETRA III). We acknowledge the European Synchrotron Radiation Facility (ESRF, Grenoble, France) for provision of synchrotron radiation facilities and we would like to thank Remi Tucoulou for assistance in using beamline ID16B for holotomography, STXM-CT and XRF-CT measurements. We acknowledge SOLEIL for provision of synchrotron radiation facilities and we would like to thank Stéphanie Belin and Valérie Briois for assistance in using beamline ROCK (proposal number 20151321). The work at ROCK was supported by a public grant overseen by the French National Research Agency (ANR) as part of the "Investissements d'Avenir" program (reference: ANR10-EQPX45).

We acknowledge KIT and DFG for financing the inVia Raman spectrometer system (INST 121384/73-1). We thank Federico Benzi for contributing during tomography experiments, Hermann Köhler (IKFT, KIT) for ICP-OES analysis, and acknowledge Evonik Industries AG for scientific discussion. Open access funding enabled and organized by Projekt DEAL.

### Conflict of Interest

The authors declare no conflict of interest.

**Keywords:** electron microscopy • Raman spectroscopy • spatially-resolved spectroscopy • X-ray microscopy • X-ray tomography

- [1] M. B. Gawande, R. K. Pandey, R. V. Jayaram, *Catal. Sci. Technol.* **2012**, *2*, 1113–1125.
- [2] J. Haber, in *Handbook of Heterogeneous Catalysis* (Eds.: G. Ertl, H. Knözinger, F. Schüth, J. Weitkamp), Wiley-VCH Verlag GmbH & Co. KGaA, Weinheim, Germany, **2008**, pp. 3359–3384.
- [3] A. Trunschke, in *Nanostructured Catalysts: Selective Oxidations* (Eds.: C. Hess, R. Schlögl), Royal Society of Chemistry, London, UK, **2011**, pp. 56–95.
- [4] A. Trunschke, J. Noack, S. Trojanov, F. Girgsdies, T. Lunkenbein, V. Pfeifer, M. Hävecker, P. Kube, C. Sprung, F. Rosowski, *ACS Catal.* **2017**, *7*, 3061–3071.
- [5] K. Weissermel, H.-J. Arpe, in *Industrial Organic Chemistry*, Wiley-VCH Verlag GmbH & Co. KGaA, Weinheim, Germany, **2008**, pp. 285–294.
- [6] P. Sprenger, T. Sheppard, J.-P. Suuronen, A. Gaur, F. Benzi, J.-D. Grunwaldt, *Catalysts* **2018**, *8*, 356–376.
- [7] I. E. Wachs, K. Routray, *ACS Catal.* **2012**, *2*, 1235–1246.
- [8] M. Wolfs, P. Batist, *J. Catal.* **1974**, *32*, 25–36.
- [9] Y. Moro-Oka, W. Ueda, *Adv. Catal.* **1994**, *40*, 233–273.
- [10] P. Sprenger, W. Kleist, J.-D. Grunwaldt, *ACS Catal.* **2017**, *7*, 5628–5642.
- [11] J. Millet, H. Ponceblanc, G. Coudurier, J. Herrmann, J. Vedrine, *J. Catal.* **1993**, *142*, 381–391.
- [12] H. Ponceblanc, J. Millet, G. Coudurier, O. Legendre, J. Vedrine, *J. Phys. Chem.* **1992**, *96*, 9462–9465.
- [13] J. F. Brazdil, *Catal. Sci. Technol.* **2015**, *5*, 3452–3458.
- [14] W. Ueda, Y. Moro-Oka, T. Ikawa, I. Matsuura, *Chem. Lett.* **1982**, *11*, 1365–1368.
- [15] Y. Moro-Oka, W. Ueda, K.-H. Lee, *J. Mol. Catal. A* **2003**, *199*, 139–148.
- [16] P. Beato, A. Blume, F. Girgsdies, R. E. Jentoft, R. Schlögl, O. Timpe, A. Trunschke, G. Weinberg, Q. Basher, F. A. Hamid, *Appl. Catal. A* **2006**, *307*, 137–147.
- [17] K. V. Raun, L. F. Lundegaard, P. Beato, C. C. Appel, K. Nielsen, M. Thorhauge, M. Schumann, A. D. Jensen, J.-D. Grunwaldt, M. Høj, *Catal. Lett.* **2019**, 1–11.
- [18] P. Sprenger, J.-D. Grunwaldt, W. Kleist, A. Fischer, *Vol. EP3219386 A1* (E. P. Office), EU, **2017**.
- [19] D. Linke, D. Wolf, M. Baerns, O. Timpe, R. Schlögl, S. Zeyß, U. Dingerdissen, *J. Catal.* **2002**, *205*, 16–31.
- [20] K. V. Raun, L. F. Lundegaard, J. Chevallier, P. Beato, C. C. Appel, K. Nielsen, M. Thorhauge, A. D. Jensen, M. Høj, *Catal. Sci. Technol.* **2018**, *8*, 4626–4637.
- [21] A. Gaur, M. Schumann, K. V. Raun, M. Stehle, P. Beato, A. D. Jensen, J. D. Grunwaldt, M. Høj, *ChemCatChem* **2019**, *11*, 4871–4883.
- [22] J. Strunk, M. A. Bañares, I. E. Wachs, *Top. Catal.* **2017**, *60*, 1577–1617.
- [23] H. Tian, I. E. Wachs, L. E. Briand, *J. Phys. Chem. B* **2005**, *109*, 23491–23499.
- [24] D. Matras, S. D. Jacques, S. Poulston, N. Grosjean, C. Estruch Bosch, B. Rollins, J. Wright, M. Di Michiel, A. Vamvakeros, R. J. Cernik, *J. Phys. Chem. C* **2019**, *123*, 1751–1760.
- [25] A. Vamvakeros, S. D. Jacques, M. Di Michiel, P. Senecal, V. Middelkoop, R. J. Cernik, A. M. Beale, *J. Appl. Crystallogr.* **2016**, *49*, 485–496.
- [26] S. D. Jacques, M. Di Michiel, A. M. Beale, T. Sochi, M. G. O'Brien, L. Espinosa-Alonso, B. M. Weckhuysen, P. Barnes, *Angew. Chem. Int. Ed.* **2011**, *50*, 10148–10152; *Angew. Chem.* **2011**, *123*, 10330–10334.

- [27] A. Vamvakeros, S. Jacques, M. Di Michiel, D. Matras, V. Middelkoop, I. Ismagilov, E. Matus, V. Kuznetsov, J. Drnec, P. Senecal, *Nat. Commun.* **2018**, *9*, 1–11.
- [28] T. Li, T. M. Heenan, M. F. Rabuni, B. Wang, N. M. Farandos, G. H. Kelsall, D. Matras, C. Tan, X. Lu, S. D. Jacques, *Nat. Commun.* **2019**, *10*, 1–11.
- [29] J. Brazdil, M. Mehicic, L. Glaeser, M. Hazle, R. Grasselli, in *Catalyst Characterization Science* (Eds.: M. L. Deviey, J. L. Gland), ACS Publications, **1985**, pp. 26–36.
- [30] B. Grzybowska-Świerkosz, *Top. Catal.* **2002**, *21*, 35–46.
- [31] O. Udalova, D. Shashkin, M. Shibanova, O. Krylov, *Kinet. Catal.* **2005**, *46*, 535–544.
- [32] N. Kumar, B. Stephanidis, R. Zenobi, A. J. Wain, D. Roy, *Nanoscale* **2015**, *7*, 7133–7137.
- [33] T. Hartman, C. S. Wondergem, N. Kumar, A. van den Berg, B. M. Weckhuysen, *J. Phys. Chem. Lett.* **2016**, *7*, 1570–1584.
- [34] K. Schuh, W. Kleist, M. Høj, V. Trouillet, P. Beato, A. D. Jensen, G. R. Patzke, J.-D. Grunwaldt, *Appl. Catal. A* **2014**, *482*, 145–156.
- [35] R. K. Grasselli, *Catal. Today* **2014**, *238*, 10–27.
- [36] H. Ponceblanc, J. Millet, G. Coudurier, J. Védrine, in *Catalytic Selective Oxidation* (Eds.: S. T. Oyama, J. W. Hightower), ACS Publications, Washington, DC, **1993**, pp. 262–272.
- [37] S. D. Jacques, M. Di Michiel, S. A. Kimber, X. Yang, R. J. Cernik, A. M. Beale, S. J. Billinge, *Nat. Commun.* **2013**, *4*, 1–7.
- [38] S. Böcklein, G. Mestl, S. V. Auras, J. Wintterlin, *Top. Catal.* **2017**, *60*, 1682–1697.
- [39] J. Engeldinger, J. Radnik, C. Kreyenschulte, F. Devred, E. M. Gaigneaux, A. Fischer, H. W. Zanthoff, U. Bentrup, *ChemCatChem* **2016**, *8*, 976–983.
- [40] M. A. Bañares, *Catal. Today* **2005**, *100*, 71–77.
- [41] O. Attila, H. E. King, F. Meirer, B. M. Weckhuysen, *Chem. Eur. J.* **2019**, *25*, 7158–7167.
- [42] A. M. Beale, S. D. Jacques, E. K. Gibson, M. Di Michiel, *Coord. Chem. Rev.* **2014**, *277*, 208–223.
- [43] J. Becher, D. F. Sanchez, D. E. Doronkin, D. Zengel, D. M. Meira, S. Pascarelli, J.-D. Grunwaldt, T. L. Sheppard, *Nat. Catal.* **2021**, *4*, 46–53.
- [44] P. Sprenger, M. Stehle, A. Gaur, A. M. Gänzler, D. Gashnikova, W. Kleist, J.-D. Grunwaldt, *ACS Catal.* **2018**, *8*, 6462–6475.
- [45] B. Ravel, M. Newville, *J. Synchrotron Radiat.* **2005**, *12*, 537–541.
- [46] P. Sprenger, T. Sheppard, J.-P. Suuronen, A. Gaur, F. Benzi, J.-D. Grunwaldt, *Catalysts* **2018**, *8*, 356.
- [47] J. Kieffer, J. Wright, *Powder Diffraction* **2013**, *28*, S339–S350.
- [48] P. P. Bruyant, *J. Nucl. Med.* **2002**, *43*, 1343–1358.
- [49] M. Basham, J. Filik, M. T. Wharmby, P. C. Chang, B. El Kassaby, M. Gerring, J. Aishima, K. Levik, B. C. Pulford, I. Sikharulidze, *J. Synchrotron Radiat.* **2015**, *22*, 853–858.
- [50] J. Schindelin, I. Arganda-Carreras, E. Frise, V. Kaynig, M. Longair, T. Pietzsch, S. Preibisch, C. Rueden, S. Saalfeld, B. Schmid, *Nat. Methods* **2012**, *9*, 676–682.

---

Manuscript received: January 11, 2021

Revised manuscript received: March 1, 2021

Accepted manuscript online: March 1, 2021

Version of record online: March 30, 2021